



Cite this: DOI: 10.1039/d5nr02117k

Modulation of quantum transport in complex oxide heterostructures with proton implantation

Haidong Liang,^{†a,b} Ganesh Ji Omar,^{†a} Kun Han,^c Andrew A. Bettiol,^{†a,b} Zhen Huang^{*,c,d} and A. Ariando^{*,a}

The interfacial electronic properties of complex oxides are governed by a delicate balance between charge transfer, lattice distortions, and electronic correlations, posing a key challenge for controlled tunability in materials research. Here, we demonstrate that proton implantation serves as a precise tool for modulating interfacial transport in SrTiO₃-based heterostructures. By introducing protons into the SrTiO₃ substrate beneath an amorphous (La,Sr)(Al,Ta)O₃ capping layer, we uncover competition between disorder and charge doping induced by implantation. At low implantation fluences below 1×10^{15} protons per cm² (1E15), the charge doping dominates, leading to an increase in carrier density and mobility, analogous to electrostatic gating effects. This enables the emergence of quantum transport oscillations at low temperature. Conversely, at higher fluences (above 1E15), disorder scattering prevails, suppressing carrier mobility and inducing an insulating state. The nonmonotonic evolution of transport with implantation fluence underscores the critical interplay between electronic correlations and disorder, offering a new paradigm for the controlled engineering of interfacial quantum states in SrTiO₃-based oxide heterostructures.

Received 20th May 2025,
Accepted 2nd November 2025

DOI: 10.1039/d5nr02117k

rsc.li/nanoscale

Introduction

Continuous efforts have been made towards developing the technique of ion implantation to fabricate commercial semiconductor devices since 1957.^{1–3} One example is the widely-used silicon-on-insulator substrate, which can be obtained using oxygen ion implantation followed by high-temperature annealing.⁴ Another example is the smart-cut process, where high-dose ion implantation is applied to create a cracking layer at a specific location to induce in-depth splitting in a target sample.⁵ Moreover, it has been demonstrated that more than 40 steps of ion implantations, with various doses and energies, are required to achieve a modern 28 nm “system on a chip” device.⁶ So, ion implantation has played an important role in developing novel functionalities and device fabrications in the Si-based industry.² On the other hand, oxide heterointerfaces are capable of integrating multiple functionalities into one device and their use has been proposed as a possible solution to preserve Moore’s law in the future.⁷ So, it is of interest

to clarify whether ion implantation, a fully-developed technique in the modern semiconductor industry, can be applied to functional oxide heterointerfaces for designing next-generation electronic devices.

A good example of functional oxide heterointerfaces is a SrTiO₃-based interface, where multiple properties including two-dimensional (2D) conductivity,^{8,9} magnetism,^{10,11} superconductivity,¹² ferroelectricity¹³ and spin–orbital coupling^{14–16} coexist. There are several reports investigating the ion-implantation effect on the well-known conducting LaAlO₃/SrTiO₃ interface. Mathew *et al.* used 2 MeV protons with doses above 6×10^{17} protons per cm² (6E17), or 500 keV He ions with doses above 1E16, to remove the interfacial conductivity of exposed areas.¹⁷ Similarly, Hurand *et al.* applied oxygen ions (50 keV, 5×10^{12} cm^{−2}) to pattern a LaAlO₃/SrTiO₃ interface to obtain a top-gated field-effect transistor, in which the micro-size channel protected from ion implantation maintains the metallic transport behavior.¹⁸ Also, Aurino *et al.* studied post thermal annealing, which heals ion-implantation-induced damage to restore the interfacial conductivity.^{19,20} All these studies focus on ion-implantation-induced *structural damage*, which creates disorders for carrier localization at the ion-implanted SrTiO₃-based interface. However, the other side of ion implantation, *charge doping*, at oxide heterointerfaces, has not been fully discussed. During ion implantation, the high-energy ions will knock out the oxygen in oxides, leaving oxygen vacancies (as localized positive charges) and excited electrons (as mobile negative charges) in SrTiO₃. It has been well docu-

^aDepartment of Physics, National University of Singapore, Singapore 117551, Singapore. E-mail: a.bettiol@nus.edu.sg, ariando@nus.edu.sg

^bCentre for Ion Beam Applications (CIBA), Department of Physics, National University of Singapore, Singapore 117542, Singapore

^cLeibniz International Joint Research Center of Materials Sciences of Anhui Province, Institutes of Physical Science and Information Technology, Anhui University, Hefei 230601, China. E-mail: huangz@ahu.edu.cn

^dStony Brook Institute at Anhui University, Anhui University, Hefei 230039, China

[†]These authors contributed equally to this work.

mented that the insulating SrTiO_3 can be easily turned into a conductor by various types of electron doping, including chemical substitutions or electrostatic gating.²¹ In this work, we will present and discuss the two sides of the ion-implantation effect, *structural damage* and *charge doping*, which simultaneously affect the SrTiO_3 -based interface.

Results and discussion

We used 50 keV protons (or H^+ in some figures) for ion implantation, and target oxide heterointerfaces were prepared by growing an amorphous $(\text{La,Sr})(\text{Al,Ta})\text{O}_3$ (*a*-LSAT) layer on a proton-implanted (001) SrTiO_3 substrate with different implantation doses. If implantation was performed after deposition, the implanted protons would traverse the already formed conducting interface and severely disrupt it, making the interface insulating. Fig. 1(a–c) show the process of sample preparation. First, the SrTiO_3 substrate was treated with buffered HF and thermal annealing to achieve an atomically flat TiO_2 -terminated surface. Second, the protons were implanted into the treated SrTiO_3 substrate with different doses, ranging from $1\text{E}14$ to $1\text{E}16$. Fig. 1(d) presents the gradual change of color in the proton-implanted SrTiO_3 substrate. When the virgin SrTiO_3 substrate (without proton implantation) is colorless and transparent, the color becomes darker and opaque with the higher implantation dose. This is because the proton implantation produces oxygen vacancies, accompanied by the formation of in-gap states to enhance the absorption of visible light in the darkened SrTiO_3 .²² Although these implanted SrTiO_3 substrates contain some oxygen vacancies, they still

maintain their insulating nature with resistance $R > 10^8 \Omega$. Third, the *a*-LSAT layer was grown on the proton-implanted SrTiO_3 substrate by pulsed laser deposition (PLD) under high-vacuum and room-temperature conditions. The high vacuum is required for the formation of an oxygen-vacancy-induced quasi-two-dimensional electron system (*q*-2DES) at the amorphous SrTiO_3 heterointerface, and room-temperature deposition is adopted to avoid the high-temperature process that could compromise the ion-implantation effect.²³ Therefore, the proton-implanted *a*-LSAT/ SrTiO_3 sample is expected to consist of two important charged regions: one is the conventional oxygen-vacancy-induced *q*-2DES close to the heterointerface (red region in Fig. 1(c)) and the other is the implanted SrTiO_3 layer (green region in Fig. 1(c)) that is far away from the heterointerface and contains implanted protons with the resulting defects.

Fig. 2 shows the basic transport properties of the *q*-2DES at the proton-implanted *a*-LSAT/ SrTiO_3 interfaces. To emphasize the modulation of proton implantation, Fig. 2(a) shows the temperature-dependent sheet resistances, obtained from samples with different proton doses, which are normalized with respect to that of the virgin sample (without proton implantation) as $R_{\text{imp}}(\text{implanted}, T)/R_{\text{vir}}(\text{virgin}, T)$. The non-normalized temperature-dependent sheet resistances of the virgin and implanted samples are provided in Fig. S1. The room-temperature sheet resistances (measured at 300 K) are monotonically reduced on increasing the proton fluence from 0 to $5\text{E}15$. However, the low-temperature sheet resistances (measured at 2 K) don't follow this monotonic trend: the low-temperature resistances reach the minimum value when the proton fluence is around $1\text{E}15$. Further increasing the implan-

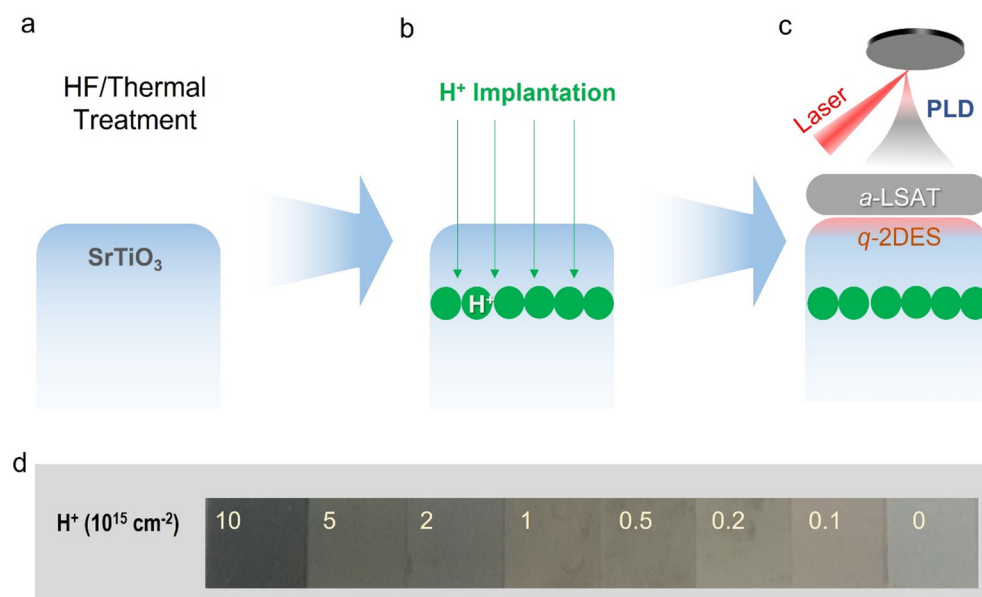


Fig. 1 Schematic of the sample preparation and optical images of the samples before and after proton implantation. (a) Buffered HF and thermal annealing treatment with the STO wafer. (b) Schematic of proton implantation in the treated STO. (c) PLD of an *a*-LSAT layer on the treated and implanted STO wafer. (d) Optical images of the STO before (rightmost, marked as 0) and after proton implantation with different doses from $1\text{E}14$ to $1\text{E}16$ (from right to left).

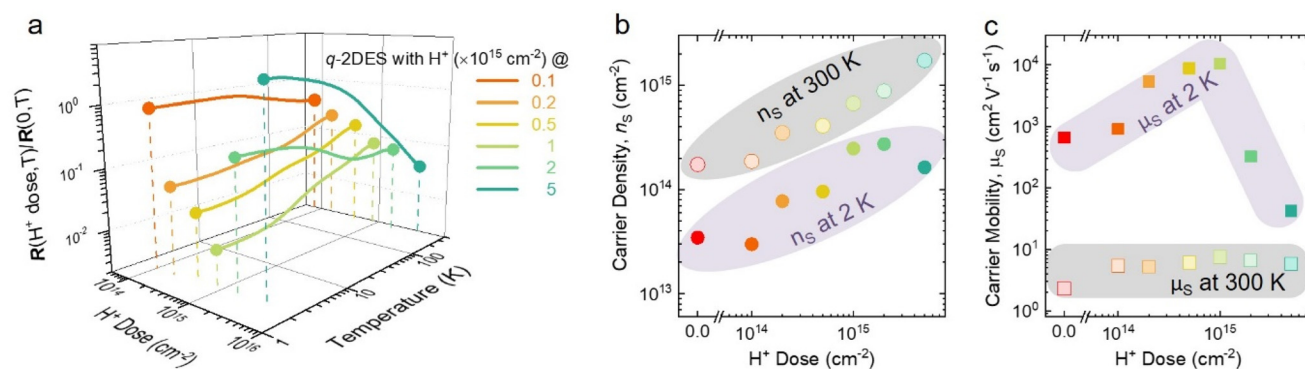


Fig. 2 Transport properties of the *a*-LSAT/SrTiO₃ interfaces. (a) Resistances of the proton implanted samples compared with that of the virgin sample. (b) Carrier densities and (c) mobilities of the virgin and implanted samples at 2 K and 300 K.

tation fluence rapidly raises the low-temperature sheet resistances, accompanied by a transition from metallic behavior ($dR/dT > 0$) to semiconducting ($dR/dT < 0$). Moreover, the sheet resistances are finally out of our measurement range ($R > 10^8 \Omega$) when the proton fluence is above 1×10^{16} , indicating insulating behavior. In Fig. 2(b), the room-temperature (300 K) and low-temperature (2 K) carrier densities n_s are plotted as functions of proton dose. Our results reveal a clear proton-implantation-induced enhancement of n_s , even in the high-fluence samples (up to 5×10^{15}) with semiconducting behaviors. Given that the implanted SrTiO₃ substrate is not conducting without the on-top *a*-LSAT layer, the observation of enhanced n_s suggests a strong interaction between two charged regions – the proton-implanted SrTiO₃ layer and the *q*-2DES interface. Also, the carrier mobilities μ_s measured at room temperature and low temperature are compared in Fig. 2(c). While the room-temperature μ_s is almost constant around $3\text{--}8 \text{ cm}^2 \text{ V}^{-1} \text{ s}^{-1}$, the low-temp-

erature μ_s is very sensitive to the proton fluence. The low-temperature μ_s reaches the maximum value $\sim 10\,000 \text{ cm}^2 \text{ V}^{-1} \text{ s}^{-1}$ with the proton fluence around 1×10^{15} , corresponding to the minimum low-temperature R . Hence, the suppression of metallic behavior in high-dose *a*-LSAT/SrTiO₃ heterointerfaces is caused by the reduction of μ_s rather than n_s .

To investigate the location of the proton-implanted layer in the SrTiO₃ substrate, Fig. 3(a) presents the simulation results obtained using SRIM (Stopping and Range of Ions in Matter).²⁴ According to the SRIM results, the end of range is at around 300 nm underneath the surface, and the proton distribution is slightly deeper than the vacancy region. Detailed SRIM results for vacancy creation are shown in Fig. S2, which suggests that most of the vacancies are oxygen vacancies.

Fig. 3(b) compares the ω - 2θ scans of X-ray diffraction (XRD) obtained from samples with different proton fluences. While the (002) peaks (indicated by a dashed line) that represent the

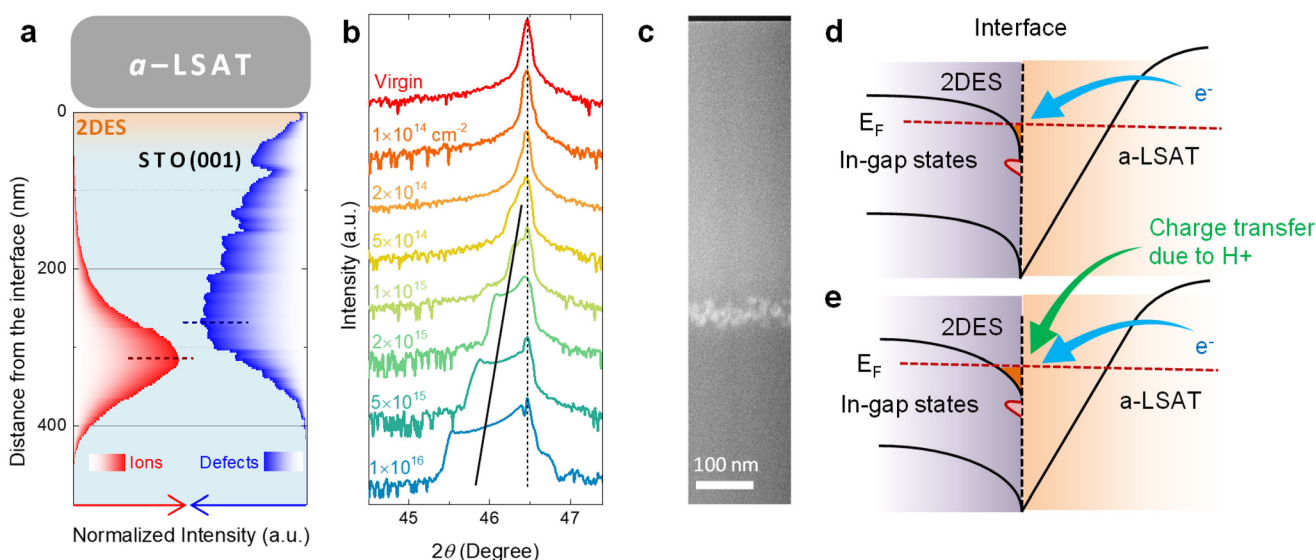


Fig. 3 Ion and vacancy distributions of the proton implanted STO wafer. (a) SRIM results of 50 keV protons in STO. (b) XRD patterns of the STO before and after proton implantation. (c) TEM image of the cross section of the irradiated STO. Band bending models of *a*-LSAT/STO with in-gap states (d) with low carrier density and (e) with higher carrier density due to H^+ charge transfer.

unaffected part of SrTiO₃ remain unchanged on increasing the proton dose, the left-side shoulders (indicated by a solid line) that result from the proton-implanted SrTiO₃ layer with defects become significant. Also, these left-side shoulders reveal the lattice expansion of proton-implanted SrTiO₃, which can be ascribed to the formation of oxygen vacancies as discussed above.^{22,25–30} On the other hand, the cross-sectional image obtained by transmission electron microscopy (TEM) reveals that the implanted SrTiO₃ layer is ~450 nm away from the *a*-LSAT/SrTiO₃ heterointerface, as shown in Fig. 3(c) and Fig. S3. The actual damage depth is deeper than the simulation result. This might be because of the channeling effect of the proton beam in the crystal lattice. Nevertheless, the fact that the proton-implanted SrTiO₃ layer is located well below the *q*-2DES layer is identified. Meanwhile, there are a limited number of disorders created at the *a*-LSAT/SrTiO₃ interface during the proton implantation that affect the *q*-2DES. It is expected that when the implantation fluence is high enough, the *structural-damage*-induced disorders will raise the energy position of the mobility edge with respect to the Fermi level (E_F , Fermi energy), leading to Anderson-localization to remove the 2D conductivity at the interface.^{31–33} The non-monotonic mobility can be rationalized within an Anderson-localization framework in which extended states exist only for energies above a disorder-dependent mobility edge energy E_C .^{34–36} By combining Hall densities with the Poisson–Schrödinger Fermi energies and fitting the low-temperature conductivity to $(E_F - E_C)^{\nu}$, we find that E_C overtakes E_F near a fluence of 1E15 (see SI Fig. S6), coincident with the observed collapse of carrier mobility.

Given the above experimental results, we proposed a model that describes the charge distribution in the proton-implanted *a*-LSAT/SrTiO₃ interface as sketched in Fig. 3(d and e). When protons are implanted into a bare SrTiO₃ substrate, oxygen vacancies (O_V) are formed to ionize the positively charged in-gap states (O_V^+) and electrons (e^-) in the proton-implanted region. Because of the surface-depletion-induced band bending as shown in Fig. 3(d), the thermally excited electrons will be easily trapped by the defect state with $O_V \rightleftharpoons O_V^+ + 2e^-$, leading to the insulating property of the proton-implanted SrTiO₃ substrate. If the SrTiO₃ surface is covered by the *a*-LSAT or *a*-LaAlO₃ layer, the surface band will bend in an opposite way to create a potential well for the *q*-2DES at the heterointerface as plotted in Fig. 3(e). In this case, electrons that are thermally excited from the defect states to the conduction band will flow to the heterointerface with $O_V \rightarrow O_V^+ + 2e^-$. To substantiate the band-bending model, we performed a self-consistent Poisson–Schrödinger estimate (SI). The calculated Fermi energy increases from ~0.05 eV in pristine interfaces to ~0.3 eV at an optimal H^+ dose, while the characteristic ground-state confinement length remains ~6–10 nm. The higher Fermi energy permits occupation of excited sub-bands, broadening the overall electron distribution and supporting the charge-transfer mechanism proposed in Fig. 3(d and e). This is consistent with our observation that both the high-temperature and low-temperature n_s increase on the proton implan-

tation. Hence, the two sides of the proton-implantation effect, including *structural damage* and *charge doping*, in the proton-implanted *a*-LSAT/SrTiO₃ heterointerface are presented. While *charge doping* plays an important role in low-fluence samples ($\leq 1E15$), the effect of *structural damage* becomes dominant on increasing the fluence ($\geq 1E16$).

Given that the ion-implantation-induced *structural damage* with high implantation doses has been well reported,^{17–19} we focus on the effect of *charge doping* in low-dose samples. As shown in Fig. 4(a and b), if the bottom implanted SrTiO₃ layer acts as the positively charged donor and the top *q*-2DES as the acceptor with negative charges, the proton-implantation-induced charge doping can be mimicked by the back-gating electrostatic doping, where additional electrons are doped into the top *q*-2DES layer by applying a positive back-gating voltage. In Fig. 4(c), the relationship between low-temperature n_s and μ_s is revealed in the proton-implanted (with fluences no more than 1E15) and back-gated *a*-LSAT/SrTiO₃ heterointerfaces. A consistent trend is observed in both cases, where the low temperature μ_s values are improved by increasing the n_s . One possible explanation is that the increased n_s enhances the screening effect to suppress the disorder-induced scattering. Another possible mechanism is that the positive charges (due to proton implantation) or voltage (from back-gating) underneath the *q*-2DES layer can draw the mobile electrons away from the interfacial defects by Coulomb interaction. Both effects mentioned above may effectively increase carrier mobilities by raising carrier densities. The similar modulation of the carrier mobility, mediated by the low-dose proton implantation and positive back-gating voltage, indicates the similar physics for charge doping in both methods.

By modifying the fluence of implanted protons, the carrier mobility of the *q*-2DES at the *a*-LSAT/SrTiO₃ interface is improved from 1000 to 10 000 cm² V⁻¹ s⁻¹. Fig. 5 presents the low temperature magneto-transport properties of the selected proton-implanted sample, and its proton fluence is 1E15 with an n_s value of 1.12×10^{14} cm⁻² and a μ_s value of 8000 cm² V⁻¹

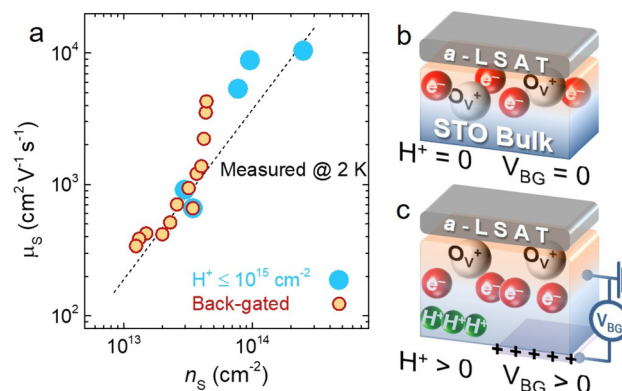


Fig. 4 Comparison of the proton implanted and back-gated induced transport. (a) Relationship between μ_s and n_s at 2 K for the ion implanted with back-gated induced transport. Schematics showing the difference in STO electron carrier density in (b) virgin and (c) implanted samples with back-gating.

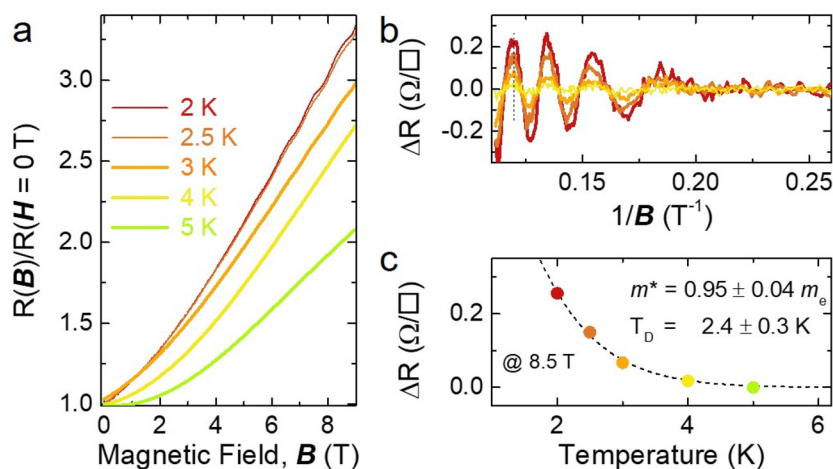


Fig. 5 Low temperature magneto-transport properties. (a) Longitudinal resistance of the selected proton-implanted sample as a function of the field for different temperatures ranging from 2 K to 5 K. (b) Inverse-field dependence of the oscillating longitudinal resistance (ΔR). (c) Temperature dependence of the longitudinal resistance (ΔR) for an 8.5 T magnetic field. Symbols are the experimental data, and solid lines are the Lifshitz–Kosevich (L–K) fits. Note: (b) and (c) follow the same colour scheme as indicated in the legend of (a). The light green colour plot (5 K) in (a) doesn't have any oscillations; therefore, it is not shown in (b).

s^{-1} . When the temperature is around 2–3 K and the magnetic field B is above 6 T, the sample shows the Shubnikov–de Haas (SdH) effect characterized by oscillating magnetoresistance; see Fig. 5(a). When plotting the low-temperature MR as a function of $1/B$, the oscillating periodicity is around 0.017 T^{-1} . The density of high-mobility electrons (n_{SdH}) that induces SdH oscillations can be estimated by $n_{\text{SdH}} = \frac{2e}{h} \sum f_i$, where f_i represents the quantum oscillation frequencies. Accordingly, n_{SdH} is $\sim 7.5 \times 10^{12} \text{ cm}^{-2}$, which is much smaller than the n_s value obtained from Hall measurements. The ratio n_{SdH}/n_s (~ 0.1 – 0.3) falls within the range reported in previous studies,^{37–41} indicating that only the light, high-mobility pockets contribute to the oscillations, while the heavier or more strongly scattered bands dominate the Hall signal. Such a phenomenon with $n_{\text{SdH}} < n_s$ is widely observed in the high-mobility q -2DES at the SrTiO₃-based heterointerface, probably due to the complicated sub-band structure associated with multiple conducting channels. It is also clearly observed that the oscillation longitudinal resistance (ΔR) decreases with increasing temperature as shown in Fig. 5(b). The oscillation longitudinal resistance (ΔR) as a function of temperature (Fig. 5(c)) can be defined as $\Delta R(T) = 4R_0 e^{-\alpha T_D/\sinh(\alpha T)}$, where $\alpha = 2\pi^2 k_B/\hbar\omega_C$, $\omega_C = eB/m^*$, k_B is the Boltzmann constant, \hbar is the Planck constant, ω_C is the cyclotron frequency, e is the elementary charge, B is the magnetic field, m^* is the carrier effective mass, R_0 is the non-oscillatory component of R_s , and T_D is the Dingle temperature. The fitting of these data by using the equation gives the effective mass $m^* = 0.95 \pm 0.04 m_e$, where m_e is the free electron mass, and Dingle temperature $T_D = 2.4 \pm 0.3 \text{ K}$. This m^* value is consistent with a moderately renormalized t_{2g} band at the α -LSAT/STO interface.^{37,42–45}

To sum up, we have shown that structural damage and charge doping—two different directions of the ion-implan-

tation effect—co-exist. An optimum proton-implanted ($1\text{E}15$ for 50 keV protons) α -LSAT/STO sample can lead high carrier mobility, which enables quantum transport oscillations at low temperature. On the other hand, samples with high implantation fluences (more than $1\text{E}15$ protons per cm^2) show signs of structural damage, which leads to reduced carrier mobility and insulating behavior. This offers a practical method for adjusting transport properties at SrTiO₃-based conducting interfaces in oxide heterostructures, opening avenues for exploring innovative functionalities.

Materials and methods

Sample preparation

The 0.5 mm thick (001) SrTiO₃ (STO) substrate (CrysTec) was treated with HF and annealed to obtain defined terrace steps and TiO₂-terminated surfaces. Substrates with proton-implantation were transferred to an ion irradiation accelerator prior to amorphous LSAT (α -LSAT) deposition. The pulsed laser deposition method was used for sample preparation. α -LSAT was grown at room temperature and in a high vacuum (10^{-6} Torr). During the growth, a nanosecond KrF 248 nm laser was used with a fluence of 2.0 J cm^{-2} and a repetition rate of 2 Hz.

Ion irradiation

A SingletonTM accelerator was used to generate H_2^+ ion beams from a hydrogen source bottle and 100 kV terminal voltage. 100 keV H_2^+ was selected by controlling a 90-degree magnetic field. The beam was focused with a quadrupole lens set to a spot size of about $50 \mu\text{m} \times 50 \mu\text{m}$ and scanned over the whole sample.⁴⁶ The irradiation fluence was controlled by the beam current and irradiation dwell time at each pixel.

Electrical measurements

Sheet resistance, carrier densities, and carrier mobility were determined using the van der Pauw method on a physical property measurement system (Quantum Design), which allowed for precise characterization of the electrical properties of the samples. Magneto-transport measurements were performed over a broad magnetic field range, up to 9 Tesla, to assess the quantum oscillation phenomenon from the transport measurements.

Conflicts of interest

There are no conflicts to declare.

Data availability

The data that support the findings of this study are available from the corresponding authors upon request.

Supplementary information (SI) is available. The Supplementary Information includes control experiments comparing different proton-implantation and a-LSAT deposition sequences, SRIM simulations of implanted-defect depth profiles, and additional TEM images of the heterostructures. It also provides the analytical framework used to quantify electronic confinement and carrier redistribution, together with the mobility-edge analysis supporting the disorder-doping crossover interpretation. DOI: <https://doi.org/10.1039/d5nr02117k>.

Acknowledgements

This research is supported by the Science and Engineering Research Council of A*STAR (Agency for Science, Technology and Research) Singapore, under Grant (M22L1b0110). The authors acknowledge financial support from the Singapore Ministry of Education (MOE) Academic Research Fund Tier 3 Grant (MOE-MOET32023-0003) "Quantum Geometric Advantage" and the Tier 2 Grants (MOE-T2EP50123-0013 and MOE-T2EP50221-0009).

References

- 1 R. B. Fair, *IEEE*, 1998, **86**, 111–137.
- 2 L. Rubin and J. Poate, *Am. Inst. Phys.*, 2003, 12–15.
- 3 W. Shockley, *U. S. Pat.*, 1957, 2,787,564.
- 4 S. Mailet, R. Stuck and J. J. G. Centre, *Nucl. Instrum. Methods Phys. Res., Sect. B*, 1987, **20**, 294–298.
- 5 M. Bruel, B. Aspar and A.-J. Auberton-Herve, *Jpn. J. Appl. Phys.*, 1997, **36**, 1636–1641.
- 6 F. Milési, J. Leveneur, V. Mazzocchi, F. Mazen, F. Gonzatti and K. Yckache, *AIP Conf. Proc.*, 2010, **1321**, 196–199.
- 7 P. Zubko, S. Gariglio, M. Gabay, P. Ghosez and J. M. Triscone, *Annu. Rev. Condens. Matter Phys.*, 2011, **2**, 141–165.
- 8 A. Ohtomo and H. Y. Hwang, *Nature*, 2004, **427**, 423–427.
- 9 S. Okamoto and A. J. Millis, *Nature*, 2004, **428**, 627–630.
- 10 A. Brinkman, M. Huijben, M. van Zalk, J. Huijben, U. Zeitler, J. C. Maan, W. G. van der Wiel, G. Rijnders, D. H. A. Blank and H. Hilgenkamp, *Nat. Mater.*, 2007, **6**, 493–496.
- 11 Ariando, X. Wang, G. Baskaran, Z. Q. Liu, J. Huijben, J. B. Yi, A. Annadi, A. R. Barman, A. Rusydi, S. Dhar, Y. P. Feng, J. Ding, H. Hilgenkamp and T. Venkatesan, *Nat. Commun.*, 2011, **2**, 1–7.
- 12 N. Reyren, S. Thiel, A. D. Caviglia, L. F. Kourkoutis, G. Hammerl, C. Richter, C. W. Schneider, T. Kopp, A.-S. Rüetschi, D. Jaccard, M. Gabay, D. A. Muller, J.-M. Triscone and J. Mannhart, *Science*, 2007, **317**, 1196–1199.
- 13 Z. Huang, Ariando, X. R. Wang, A. Rusydi, J. Chen, H. Yang and T. Venkatesan, *Adv. Mater.*, 2018, **30**, 1–22.
- 14 J. Varignon, L. Vila, A. Barthélémy and M. Bibes, *Nat. Phys.*, 2018, **14**, 322–325.
- 15 M. Ben Shalom, M. Sachs, D. Rakhmilevitch, A. Palevski and Y. Dagan, *Phys. Rev. Lett.*, 2010, **104**, 1–4.
- 16 G. J. Omar, W. L. Kong, H. Jani, M. S. Li, J. Zhou, Z. S. Lim, S. Prakash, S. W. Zeng, S. Hooda, T. Venkatesan, Y. P. Feng, S. J. Pennycook, L. Shen and A. Ariando, *Phys. Rev. Lett.*, 2022, **129**, 1–6.
- 17 S. Mathew, X. A. Annadi, X. T. K. Chan, T. C. Asmara, D. Zhan and M. E. T. Al, *ACS Nano*, 2013, 10572–10581.
- 18 S. Hurand, A. Jouan, C. Feuillet-Palma, G. Singh, E. Lesne, N. Reyren, A. Barthélémy, M. Bibes, J. E. Villegas, C. Ulysse, M. Pannetier-Lecoeur, M. Malnou, J. Lesueur and N. Bergeal, *Appl. Phys. Lett.*, 2016, **108**, 052602.
- 19 P. P. Aurino, A. Kalabukhov, N. Tuzla, E. Olsson, A. Klein, P. Erhart, Y. A. Boikov, I. T. Serenkov, V. I. Sakharov, T. Claeson and D. Winkler, *Phys. Rev. B:Condens. Matter Phys.*, 2015, **92**, 3–11.
- 20 P. P. Aurino, A. Kalabukhov, N. Tuzla, E. Olsson, T. Claeson and D. Winkler, *Appl. Phys. Lett.*, 2013, **102**, 1–4.
- 21 Y.-Y. Pai, A. Tylan-Tyler, P. Irvin and J. Levy, *Rep. Prog. Phys.*, 2018, **81**, 036503.
- 22 H. N. Lee, S. S. Ambrose Seo, W. S. Choi and C. M. Rouleau, *Sci. Rep.*, 2016, **6**, 1–7.
- 23 G. J. Omar, M. Li, X. Chi, Z. Huang, Z. S. Lim, S. Prakash, S. Zeng, C. Li, X. Yu, C. Tang, D. Song, A. Rusydi, T. Venkatesan, S. J. Pennycook and A. Ariando, *Nano Lett.*, 2020, **20**, 2493–2499.
- 24 J. F. Ziegler, M. D. Ziegler and J. P. Biersack, *Nucl. Instrum. Methods Phys. Res., Sect. B*, 2010, **268**, 1818–1823.
- 25 Y. Li, Y. Lei, B. G. Shen and J. R. Sun, *Sci. Rep.*, 2015, **5**, 1–7.
- 26 S. A. Lee, H. Jeong, S. Woo, J. Y. Hwang, S. Y. Choi, S. D. Kim, M. Choi, S. Roh, H. Yu, J. Hwang, S. W. Kim and W. S. Choi, *Sci. Rep.*, 2016, **6**, 1–10.
- 27 K. Song, T. Min, J. Seo, S. Ryu, H. Lee, Z. Wang, S. Y. Choi, J. Lee, C. B. Eom and S. H. Oh, *Adv. Sci.*, 2021, **8**, 1–12.
- 28 G. Panomsuwan and N. Saito, *Oxygen*, 2021, **1**, 62–72.
- 29 Y. Li, S. J. Peng, T. T. Mao, D. J. Wang, K. M. Wu, J. R. Sun and J. Zhang, *AIP Adv.*, 2017, **7**, 055821.

- 30 Q. Lu, C. Sohn, G. Hu, X. Gao, M. F. Chisholm, I. Kylänpää, J. T. Krogel, P. R. C. Kent, O. Heinonen, P. Ganesh and H. N. Lee, *Sci. Rep.*, 2020, **10**, 1–7.
- 31 T. Fix, F. Schoofs, J. L. MacManus-Driscoll and M. G. Blamire, *Phys. Rev. Lett.*, 2009, **103**, 1–4.
- 32 Z. Huang, X. R. Wang, Z. Q. Liu, W. M. Lü, S. W. Zeng, A. Annadi, W. L. Tan, X. P. Qiu, Y. L. Zhao, M. Salluzzo, J. M. D. Coey, T. Venkatesan and Ariando, *Phys. Rev. B: Condens. Matter Mater. Phys.*, 2013, **88**, 1–5.
- 33 I. Pallecchi, F. Telesio, D. Li, A. Fête, S. Gariglio, J. M. Triscone, A. Filippetti, P. Delugas, V. Fiorentini and D. Marré, *Nat. Commun.*, 2015, **6**, 1–7.
- 34 Z. S. Popović, S. Satpathy and R. M. Martin, *Phys. Rev. Lett.*, 2008, **101**, 1–4.
- 35 M. Kolodrubetz and B. K. Clark, *Phys. Rev. B: Condens. Matter Mater. Phys.*, 2012, **86**, 1–11.
- 36 J. S. Lee, Y. W. Xie, H. K. Sato, C. Bell, Y. Hikita, H. Y. Hwang and C. C. Kao, *Nat. Mater.*, 2013, **12**, 703–706.
- 37 C. Cancellieri, A. S. Mishchenko, U. Aschauer, A. Filippetti, C. Faber, O. S. Barišić, V. A. Rogalev, T. Schmitt, N. Nagaosa and V. N. Strocov, *Nat. Commun.*, 2016, **7**, 10386.
- 38 N. Scopigno, D. Bucheli, S. Caprara, J. Biscaras, N. Bergeal, J. Lesueur and M. Grilli, *Phys. Rev. Lett.*, 2016, **116**, 1–5.
- 39 A. Joshua, S. Pecker, J. Ruhman, E. Altman and S. Ilani, *Nat. Commun.*, 2012, **3**, 1129.
- 40 A. Fête, C. Cancellieri, D. Li, D. Stornaiuolo, A. D. Caviglia, S. Gariglio and J.-M. Triscone, *Appl. Phys. Lett.*, 2015, **106**, 051604.
- 41 S. Fernandez-Peña, C. Lichtensteiger, P. Zubko, C. Weymann, S. Gariglio and J.-M. Triscone, *APL Mater.*, 2016, **4**, 086105.
- 42 M. Ben Shalom, C. W. Tai, Y. Lereah, M. Sachs, E. Levy, D. Rakhmilevitch, A. Palevski and Y. Dagan, *Phys. Rev. B: Condens. Matter Mater. Phys.*, 2009, **80**, 3–6.
- 43 A. Janotti and C. G. Van De Walle, *Phys. Rev. B: Condens. Matter Mater. Phys.*, 2007, **76**, 1–22.
- 44 J. L. M. Van Mechelen, D. Van Der Marel, C. Grimaldi, A. B. Kuzmenko, N. P. Armitage, N. Reyren, H. Hagemann and I. I. Mazin, *Phys. Rev. Lett.*, 2008, **100**, 7–10.
- 45 J. T. Devreese and A. S. Alexandrov, *Rep. Prog. Phys.*, 2009, **72**, 066501.
- 46 H. Liang, Y. Zheng, L. Loh, Z. Hu, Q. Liang, C. Han, M. Bosman, W. Chen and A. A. Bettiol, *Nano Res.*, 2022, **16**, 1220–1227.